ELSEVIER

Contents lists available at ScienceDirect

Chemical Engineering Science

journal homepage: www.elsevier.com/locate/ces



Description of confined nanoflow transport considering the effects of capillary condensation and heat transfer by means of a two-phase lattice Boltzmann model

Javad Sodagar-Abardeh 🕩*, Thomas Loimer 🕩

Institute of Fluid Mechanics and Heat Transfer, Vienna University of Technology, Austria

ARTICLE INFO

Keywords: Mesoscale simulation Lattice Boltzmann method Two-phase flow Capillary condensation effect

ABSTRACT

The pseudopotential two-phase Lattice Boltzmann method is used to study a flow with condensation and evaporation through slits ranging between 8 to 24 nm in width by applying a pressure gradient. The slits are about 700 nm long. The fluid described by the Carnahan-Starling equation of state is in the form of a vapor upstream of the pore. For the smaller applied pressure gradient, the vapor flows through the slit. However, for higher values of the pressure gradient, as the gas flows through the slit, the fluid condenses, and consequently, liquid flows through the slit. The liquid may leave the slit, or it evaporates. Here, the condition at the interface between the liquid and the gaseous flow region, where mass transfer by evaporation takes place, is investigated. The pressure difference across the curved meniscus is consistent with the Young-Laplace equation and nearly independent of the mass flow rate. However, the curvature of the interface depends on the strength of the fluid-wall interaction. The curvature of the meniscus and effects influencing the curvature play an important role in the process. Considering the temperature field in the transport process reveals that different boundary conditions for the domain influence the mass flow rate. Heating the slit from the downstream side decreases the mass flow rate.

1. Introduction

The transport of fluids in nanopores under nonequilibrium conditions has been studied extensively in both experiments and theory (Wang and Aryana, 2021; Huang et al., 2021; Song et al., 2020; Yu et al., 2018; Namadchian et al., 2022). Membrane separations have great potential in this area (Phan et al., 2020). By operating under specific conditions and taking advantage of the adsorption and capillary condensation phenomena, which result in selectivity and high permeability, the potential for gas separations increases considerably inside the nanoporous structure (Yabunaka and Fujitani, 2022; Deng et al., 2023). It is worth noting that under these operational conditions, the transportation of vapors takes place within the pressure range where capillary condensation occurs.

To date, the study of fluid transport at the nanoscale has involved experimental investigations, improved thermodynamic models, and numerical simulations. Uchytil et al. (2003, 2005) examined the permeation of butane and isobutane through Vycor nanoporous glass. They attempted to demonstrate a correlation between the inlet and exit bulk pressure conditions and the observed experimental permeation

behavior. It was assumed that these conditions have an impact on the state of the fluid within the nanoporous medium.

The existing limitations of the experimental apparatus restrict us from confirming and exploring these conditions at a microscopic level. Nonetheless, there were several attempts to connect these states to measurable quantities such as flux, pressure, and mesoporous structure through transportation models. Loimer et al. (2011, 2023) employed a combination of the Hagen-Poiseuille model, which describes liquid flow, and the Knudsen diffusion model, which describes gas flow, to clarify situations where there is a two-phase flow within anodized alumina membranes. However, it is important to note that this study focuses on capturing the effects of capillary condensation, where viscous flow dominates the transport mechanism. A more accurate description of gaseous flow, including the Knudsen effect, remains to be explored in future work. If liquid flows through part of the pore, the effect of the interface between the liquid and the gaseous flow region usually dominates the flow.

Recently, the comprehension of the thermodynamics of fluids within the nanoconfined mesoporous materials has significantly improved, mainly concerning capillary transitions, owing to the improvements

E-mail addresses: javad.sodagar@tuwien.ac.at (J. Sodagar-Abardeh), thomas.loimer@tuwien.ac.at (T. Loimer).

^{*} Corresponding author.

in molecular simulation techniques (Monson, 2012; Sun et al., 2020). Numerical simulation in this scale allows for investigating many fluid types across a wide range of pressure or temperature conditions. While molecular dynamic simulation is effective at uncovering novel phenomena on the nanoscale by modeling the movement of each molecule, it is computationally expensive. Besides the method that operates at a molecular level, classical density functional theory (DFT) is also effective in conducting theoretical examinations of the thermodynamic properties of fluids within nanopores. Li and Firoozabadi (2009) integrated DFT and the Peng-Robinson equation of state (EOS) to simulate the interfacial tension of pure substances and binary mixtures. Jin and Firoozabadi (2016), Li et al. (2014), and Liu et al. (2018) applied DFT to analyze the adsorption and behavior of confined phases in nanoslits. The results indicated a suppressed critical temperature and an increased critical density, which are qualitatively in line with findings from molecular simulations. Furthermore, dynamic mean field theory has been developed to extend this method, allowing for the study of nanofluid transport (Edison and Monson, 2013, 2012). Rathi et al. (2019) used dynamic mean field theory and molecular dynamics to examine the transportation of condensable fluids in nanoporous membranes under nonequilibrium conditions. A single-slit pore represented the model to simplify the complexity of the transport mechanism. The study compared the dynamics of a system that began in an initial equilibrium state to that of approaching another equilibrium or nonequilibrium state. This approach allowed for an evaluation of the transportation process in a controlled and decoupled environment.

To account for the effects of confinement, researchers have developed modified EOS that incorporate additional parameters or modifications to the existing parameters. For example, one approach is to shift the critical point of the EOS to account for the effect of confinement (Zarragoicoechea and Kuz, 2004). This is because confinement can alter the thermodynamic properties of the fluid and shift the value of the critical point. Another approach is to couple the capillary pressure to the EOS, which allows for the effects of the pore size and shape on the fluid behavior to be considered (Liu et al., 2018).

We can understand the physics behind flow and transport at a microscale using molecular dynamics (MD) simulations. However, simulating more complex fluids or larger systems becomes difficult due to the expensive computational cost and complexities required for MD force field simulations. Additionally, while molecular-level research offers valuable insights into confined phase behavior, applying this knowledge to thermodynamic models to make predictions is challenging. To address these issues, one potential solution is to use insights gained from MD simulations to create a mesoscopic computational model. The possible method needs to adequately capture the physics at a small scale and allow for the scaling of the system from a microscopic to a macroscopic level. As a mesoscopic approach, the lattice Boltzmann Method (LBM) will enable us to directly bridge the gap between microscale kinetics and macroscale properties (Bao and Guo, 2024; Pasieczynski and Chen, 2020; Albernaz et al., 2015). Compared to DFT, the LBM can capture the dynamic phase transition process and requires less computational time than MD or Monte Carlo simulations (Huang et al., 2021). Among the several two-phase LBM approaches available, the pseudopotential model is a popular choice due to its simplicity and ability to implement interactive forces directly through pseudopotential functions (Areshi et al., 2024). Yuan and Schaefer (2006) linked various equations of state to pseudopotential functions and simulated phase behavior for real gases. Although the original pseudopotential model is not thermodynamically consistent (Huang et al., 2021), many studies have used modified versions of the model to simulate confined phase behavior (Sodagar-Abardeh et al., 2023). To investigate how confined phase behavior affects the transport of methane in slit nanopores, Wang and Aryana (2021) used a modified EOS in combination with a multi-relaxation time LBM. They estimated the transport properties by examining the mass flux profiles. Recently, machine learning techniques such as Symbolic Regression and Genetic Programming have been employed to develop surrogate models that capture complex physical behaviors with simplified analytical expressions. These approaches offer high accuracy, interpretability, and the potential to uncover underlying physical laws from simulation or experimental data (Khadem and Rey, 2021; Khadem et al., 2014).

Following our previous work on the equilibrium phase behavior of fluids in confined nanopores, in the present work we employ a thermal two-phase lattice Boltzmann method to study the transport phenomena of condensable gas in nanoporous membranes under nonequilibrium conditions by allowing variations of the temperature. To the best of our knowledge, this is the first time the lattice Boltzmann approach has been used to accurately capture the nonequilibrium steady state properties of pressure-driven two-phase flow transport within a slit confinement. Building upon our previous study (Sodagar-Abardeh et al., 2023), we conducted a comparative investigation of the dynamics of a system starting from an initial equilibrium state approaching a nonequilibrium (or an equilibrium) state. Specifically, we investigated the effect of the nanoslit width and the temperature fields on the mass flow rate. We also evaluated the deviation of gas pressure at the downstream meniscus with respect to the equilibrium state when there is a flow across the meniscus. Our findings offer insights into the transport of fluids in nanopores and can also be extended to more complex nanoporous media, such as media with parallel pore network structures.

2. Model description

2.1. Double distribution two-phase lattice Boltzmann method

The double distribution two-phase lattice Boltzmann method (DD-TLBM) is a simulation technique that can model fluid flow and temperature fields in a two-phase system. This method uses two sets of distribution functions, where one of them represents the velocity of the fluid and the density which connects to the pressure through EOS. The other distribution function can represent various physical quantities, such as temperature or concentration, depending on the specific application being modeled. In the case of a two-phase flow problem involving heat transfer, the second distribution can be used to represent the temperature field (Qin et al., 2019).

2.1.1. First distribution function: Density field

The first distribution function of DD-TLBM calculates the macroscopic characteristics of a fluid flow by tracking the changes in the probability distribution function of density at each lattice. This discrete distribution function is governed by the following equation (Sodagar-Abardeh et al., 2023):

$$f_i(\mathbf{r} + \mathbf{c}_i \Delta t, t + \Delta t) = \left(1 - \frac{\Delta t}{\tau}\right) f_i(\mathbf{r}, t) + \frac{\Delta t}{\tau} f_i^{\text{eq}}(\mathbf{r}, t) + \Delta f_i. \tag{1}$$

The probability distribution function $f_i(\mathbf{r},t)$ in the above relation is associated with the discrete velocity vector \mathbf{c}_i of the lattice located at \mathbf{r} and time t. In Eq. (1), $f_i^{\rm eq}(\mathbf{r},t)$ is the equilibrium distribution function, which is fully defined in Eq. (4), and τ represents the relaxation time. The change in the equilibrium distribution function caused by an external body force is represented by Δf_i , and this transformation is detailed in Eq. (7). The macroscopic density and velocity of the fluid can be calculated by evaluating the zeroth and first moments of the density distribution function, respectively,

$$\rho(\mathbf{r},t) = \sum_{i=0}^{n} f_i(\mathbf{r},t), \tag{2}$$

$$\mathbf{u}(\mathbf{r},t) = \frac{\sum_{i=0}^{n} \mathbf{c}_{i} f_{i}(\mathbf{r},t)}{\rho(\mathbf{r},t)}.$$
 (3)

In Eq. (2), n refers to the number of directions in which the probability function can stream, and this equation represents the zeroth moment of the density distribution function. As previously stated in Eq. (1), the

symbol $f_i^{\rm eq}({\bf r},t)$ represents the equilibrium distribution function, which is defined by

$$f_i^{\text{eq}}(\mathbf{r},t) = \rho(\mathbf{r},t)\omega_i \left[1 + \frac{\left(\mathbf{c}_i \cdot \mathbf{u}(\mathbf{r},t) \right)}{c_s^2} + \frac{\left(\mathbf{c}_i \cdot \mathbf{u}(\mathbf{r},t) \right)^2}{2c_s^4} + \frac{\mathbf{u}(\mathbf{r},t) \cdot \mathbf{u}(\mathbf{r},t)}{2c_s^2} \right]. \tag{4}$$

The equilibrium distribution function, expressed in Eq. (4), includes the weighting factor ω_i and the speed of sound in the lattice space c_s . Numerical simulations in the present work were conducted in a two-dimensional domain and nine-directions known as the D2Q9 scheme for the density field. For this scheme, the weighting coefficients and the discrete velocity vectors are provided by

$$\omega_{i} = \begin{cases} \frac{16}{36} & i = 0\\ \frac{4}{36} & i = 1 : 4, \quad \mathbf{c}_{i} = \begin{cases} -2mm(0,0) & i = 0\\ (\pm 1,0), (0,\pm 1) & i = 1 : 4\\ (\pm 1,\pm 1) & i = 5 : 8 \end{cases}$$
 (5)

Where the tuples (x,y) represent the direction in Cartesian x- and y-coordinates. The relationship between the relaxation time and the fluid viscosity as one of the macroscopic properties can be determined using a multi-scale Chapman-Enskog expansion, which is expressed as

$$v_{\rm LBM} = c_s^2 \left(\tau - \frac{\Delta t}{2}\right). \tag{6}$$

Here, the kinematic viscosity of the fluid in the lattice unit is denoted by $v_{\rm LBM}$. Although a single-relaxation-time scheme is used, different values of the relaxation time τ are applied for the liquid and vapor phases, denoted by $\tau_{\rm liq}$ and $\tau_{\rm vap}$, respectively. In the interfacial region, where the density transitions smoothly between phases, a linear interpolation is used to assign an effective relaxation time based on the local density. The exact difference method, proposed by (Kupershtokh and Medvedev, 2006), is used to incorporate external forces into the current model. By applying this approach, the change in the equilibrium distribution function resulting from the external body force is added to the right-hand side of Eq. (1), as given by

$$\Delta f_i = f_i^{\text{eq}}(\rho(\mathbf{r}, t), (\mathbf{u} + \Delta \mathbf{u})(\mathbf{r}, t)) - f_i^{\text{eq}}(\rho(\mathbf{r}, t), \mathbf{u}(\mathbf{r}, t)). \tag{7}$$

When the external body force is included during the time increment, it leads to a change in velocity, which is represented as

$$\Delta \mathbf{u}(\mathbf{r},t) = \frac{\Delta t \, \mathbf{f}^{\text{total}}(\mathbf{r},t)}{\rho(\mathbf{r},t)},
\mathbf{f}^{\text{total}}(\mathbf{r},t) = \mathbf{F}^{\text{g}}(\mathbf{r},t) + \mathbf{F}^{\text{cohesive}}(\mathbf{r},t) + \mathbf{F}^{\text{adhesive}}(\mathbf{r},t).$$
(8)

Here, $\mathbf{F}^{\text{total}}$ represents the total external force, which is composed of the cohesive force (fluid-fluid interaction) represented by $\mathbf{F}^{\text{cohesive}}$, the adhesive force (fluid-solid interaction) represented by $\mathbf{F}^{\text{adhesive}}$, and the gravitational force represented by \mathbf{F}^g . The actual fluid velocity can be calculated using the equation

$$\mathbf{u}_{\text{real}}(\mathbf{r},t) = \mathbf{u}(\mathbf{r},t) + \frac{\Delta t \,\mathbf{F}^{\text{total}}(\mathbf{r},t)}{2\rho(\mathbf{r},t)}.\tag{9}$$

2.1.2. Interaction forces: Phase transition and wettability

In the pseudopotential Lattice Boltzmann method, it is assumed that a particle exists at each lattice location. Interaction forces between these pseudo-particles of the working fluid are modeled and allow the model to describe phase transition. The interaction forces between lattices representing different materials will enable us to describe wettability. Eqs. (10) and (11) illustrate the cohesive force between fluid-fluid particles and the adhesive force between fluid-solid particles, respectively,

$$\mathbf{F}^{\text{cohesive}}(\mathbf{r},t) = -\beta G_{\text{cohesive}} \psi(\mathbf{r},t) \sum_{i=1}^{n} \omega^{\mathbf{F}} \left(\left| \mathbf{c}_{i} \right|^{2} \right) \psi(\mathbf{r} + \mathbf{c}_{i} \Delta t, t) \mathbf{c}_{i}$$

$$- \frac{1 - \beta}{2} G_{\text{cohesive}} \sum_{i=1}^{n} \omega^{\mathbf{F}} \left(\left| \mathbf{c}_{i} \right|^{2} \right) \psi^{2} \left(\mathbf{r} + \mathbf{c}_{i} \Delta t, t \right) \mathbf{c}_{i}, \tag{10}$$

$$\mathbf{F}^{\text{adhesive}}(\mathbf{r},t) = -G_{\text{adhesive}} \psi(\mathbf{r},t) \sum_{i=1}^{9} \omega^{\mathbf{F}} \left(\left| \mathbf{c}_{i} \right|^{2} \right) S(\mathbf{r} + \mathbf{c}_{i} \Delta t, t) \mathbf{c}_{i}.$$
 (11)

Regarding the relation for the cohesive interaction, the strength of the fluid-fluid interaction is represented by G_{cohesive} , while the tunable parameter β is used to increase the isotropic order, and ω^{F} denotes the weighting factor. Notably, only cohesive interactions between particles in the nearest adjacent lattices are considered. For D2Q9, G_{cohesive} has a constant value of 1, and the weighting factors are given by $\omega^{\text{F}}(0)=0,\ \omega^{\text{F}}(1)=\frac{1}{3},\ \text{and}\ \omega^{\text{F}}(0)=\frac{1}{12}.$ The isotropic order of the interaction force in the first distribution of DD-TLBM has an impact on the fluid density at lower temperatures, particularly close to an interface where the gradient of density is large, according to Huang et al. (2021). To align the model's predictions with classical thermodynamics relations, the constant β needs to be adjusted appropriately.

The cohesive force's value at the domain's entrance and exit should be approximated to implement the boundary conditions properly. Based on Eq. (10), the value of the potential function $\psi(x)$ for the neighbor nodes $(\psi(x+1))$ and $\psi(x-1)$ should be known to approximate the cohesive interaction. The interaction force must be computed differently at those boundaries when using boundary conditions (e.g., constant pressure) because three nodes (for the D2Q9 arrangement) are unavailable. In the present model, the forward and backward space derivation is implemented in the numerical model to approximate the cohesive force at the entrance and exit. To implement the cohesive interaction for the interior nodes, the first-order space derivative of the potential function $\psi(x)$ is evaluated in an isotropic central scheme (second-order accuracy) as follows:

$$\frac{\partial \psi}{\partial x} \approx \frac{1}{3} (\psi_{i+1,j} - \psi_{i-1,j}) + \frac{1}{12} (\psi_{i+1,j+1} - \psi_{i-1,j+1} + \psi_{i+1,j-1} - \psi_{i-1,j-1}).$$

$$\frac{\partial \psi}{\partial y} \approx \frac{1}{3} (\psi_{i,j+1} - \psi_{i,j-1}) + \frac{1}{12} (\psi_{i+1,j+1} - \psi_{i+1,j-1} + \psi_{i-1,j+1} - \psi_{i-1,j-1}).$$
(12)

For the inlet boundary nodes, the isotropic forward scheme is used in the x direction as follows:

$$\frac{\partial \psi}{\partial x} \approx \frac{1}{3} (-3\psi_{i,j} + 4\psi_{i+1,j} - \psi_{i+2,j}) + \frac{1}{12} (-3\psi_{i,j+1} + 4\psi_{i+1,j+1} - \psi_{i+2,j+1} - 3\psi_{i,j-1} + 4\psi_{i+1,j-1} - \psi_{i+2,j-1}).$$
(13)

For the outlet boundary nodes, the isotropic backward scheme is used in x direction as follows:

$$\frac{\partial \psi}{\partial x} \approx \frac{1}{3} (3\psi_{i,j} - 4\psi_{i-1,j} + \psi_{i-2,j}) + \frac{1}{12} (3\psi_{i,j+1} - 4\psi_{i-1,j+1} + \psi_{i-2,j+1} + 3\psi_{i,i-1} - 4\psi_{i-1,i-1} + \psi_{i+2,i-1}).$$
(14)

With regards to the adhesive force given in Eq. (11), the adhesive strength is characterized by $G_{\rm adhesive}$, which is determined by aligning the density ratio, defined as the ratio of the density near the wall to that at the slit centerline. A common approach to determine this constant involves calibrating the results from the Lattice Boltzmann Method against those from Molecular Dynamics simulations under identical pressure and temperature conditions (Wang and Aryana, 2021). Additionally, by modifying this constant, the DD-TLBM model can produce different contact angles. The index function $S(\mathbf{r}+\mathbf{c}_i\Delta t,t)$ is defined as 1 for solid nodes and 0 for fluid nodes. In Eqs. (10) and (11), the potential function is denoted by $\psi_{(\mathbf{r},t)}$.

In the present model, the fluid pressure is expressed by

$$P(\mathbf{r},t) = c_s^2 \rho(\mathbf{r},t) + \frac{1}{2} G_{\text{cohesive}} c_0 \psi^2(\mathbf{r},t), \tag{15}$$

where the constant $G_{\rm cohesive}$ determines the strength of interaction, and the value of c_0 for the D2Q9 scheme is 6. Moreover, in this study the Carnahan-Starling EOS is used as a non-ideal EOS to describe the

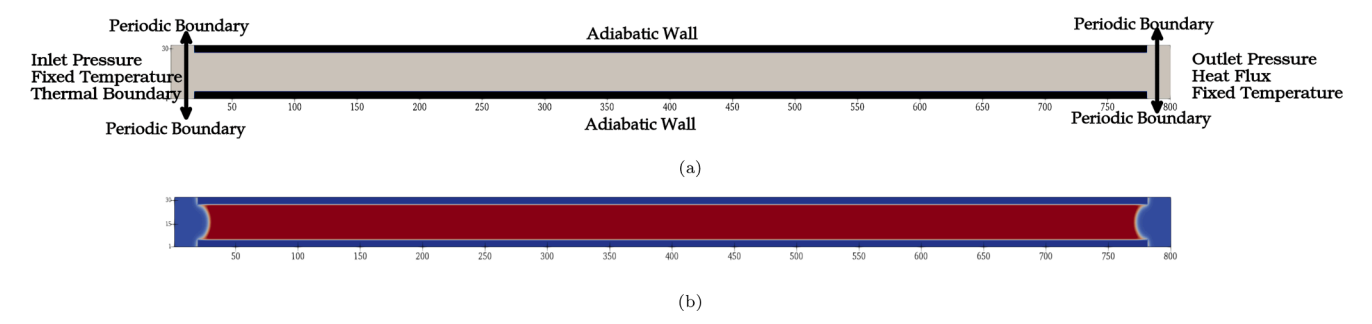


Fig. 1. a) Schematic of domain and boundary conditions for the numerical simulations. b) Equilibrium density distribution: red represents the liquid phase, blue represents the vapor phase, serving as the initial condition for the nonequilibrium solver.

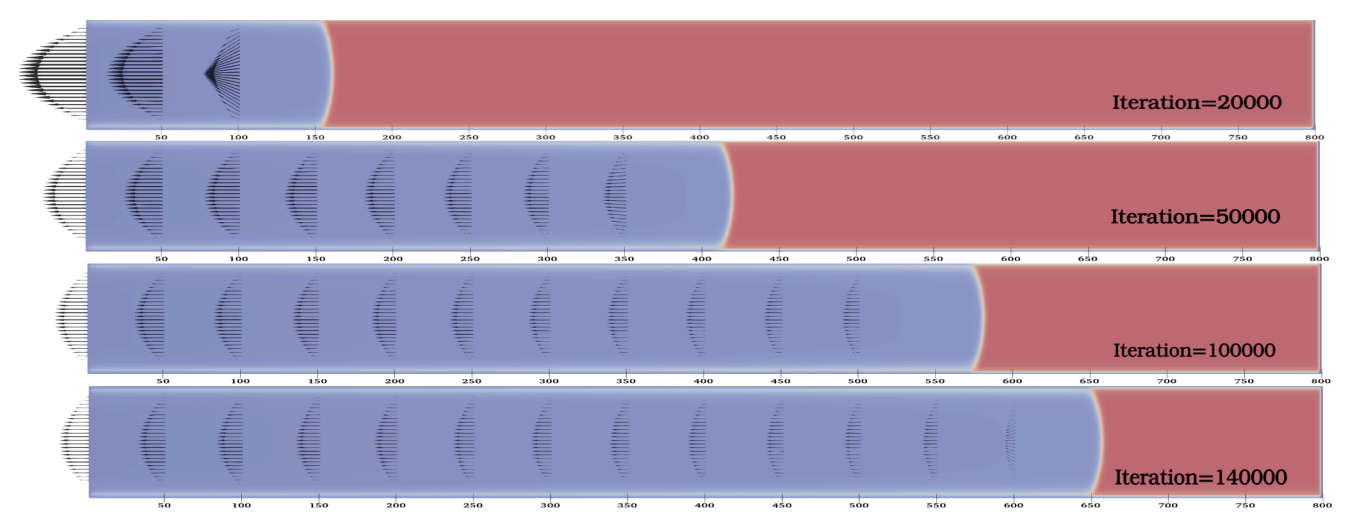


Fig. 2. An illustration depicting the validation case that simulates the evaporation of the fluid within a nanotube for the adhesive strength $G_{\text{adhesive}} = 0.4$.

pressure within the fluid field. This non-ideal EOS is expressed as

$$P(\mathbf{r},t) = \frac{\rho(\mathbf{r},t)RT\left(1 + (b\rho(\mathbf{r},t)/4) + (b\rho(\mathbf{r},t)/4)^2 - (b\rho(\mathbf{r},t)/4)^3\right)}{(1 - (b\rho(\mathbf{r},t)/4))^3}$$
$$-a\rho^2(\mathbf{r},t), \tag{16}$$

where the pressure, absolute temperature, and gas constant are represented by P, T, and R, respectively. The repulsion parameter, $b \ (0.18727RT_{\rm c}/p_{\rm c})$, and the attraction parameter, $a \ (0.4963R^2T_{\rm c}^2/p_{\rm c})$, are set to 4 and 1, respectively. The reduced pressure and temperature in lattice unit is $p_{\rm c}=0.00442$ and $T_{\rm c}=0.094$, respectively. From Eq. (16), the pressure can be computed at each lattice node. Substituting the pressure in Eq. (15), we can calculate the potential function $\psi({\bf r},t)$ at each lattice node as follows,

$$\psi(\mathbf{r},t) = \left(2\left(\frac{\rho(\mathbf{r},t)RT(1+(\left(b\rho(\mathbf{r},t)/4\right)+(b\rho(\mathbf{r},t)/4)^2-(b\rho(\mathbf{r},t)/4)^3)}{(1-(b\rho(\mathbf{r},t)/4))^3}\right) - a\rho^2(\mathbf{r},t) - c_s^2\rho(\mathbf{r},t)\right)/G_{\text{cohesive}}c_0\right)^{0.5}.$$
(17)

2.1.3. Second distribution function: Temperature field

In the thermal two-phase Lattice Boltzmann method, the second set of distributions representing the temperature field is related to the first distribution, i.e., the density field, through the EOS. Assuming that there is no heat dissipation due to viscosity, the governing equation for the second distribution function of DD-TLBM model can be expressed in the following manner (Zarghami and Van den Akker, 2017; Kamali et al., 2013; Zarghami et al., 2015):

$$g_i(\mathbf{r} + \mathbf{c}_i \Delta t, t + \Delta t) - g_i(\mathbf{r}, t) = \frac{\Delta t}{\tau_g} (g_i(\mathbf{r}, t) - g_i^{\text{eq}}(\mathbf{r}, t)) + \omega_i^T G^{\text{ext}}.$$
 (18)

Here g_i denotes the thermal distribution function, τ_g is the thermal relaxation time, $G^{\rm ext}$ is an external source term, and g_i^{eq} denotes the equilibrium thermal distribution function given by

$$g_i^{\text{eq}}(\mathbf{r},t) = T(\mathbf{r},t)\omega_i^{\text{T}} \left[1 + \frac{\mathbf{c}_i \cdot \mathbf{u}_{\text{real}}(\mathbf{r},t)}{c_s^2} \right].$$
 (19)

Here, $T(\mathbf{r},t) = \sum_{i=0}^{n} g_i(\mathbf{r},t)$ is the temperature of each lattice at time t.

By using the D2Q5 scheme in the current DD-LBM model, one can simulate the nonisothermal two-phase flow transport phenomena in nanochannels while keeping the computational cost manageable. The D2Q5 model uses five discrete velocities to represent the probability of finding the temperature of a specific lattice on the domain. ω_i^T represents the thermal weighting factor for the *i*-th discrete velocity,

$$\omega_i^T = \begin{cases} \frac{1}{3} & i = 0\\ \frac{1}{6} & i = 1:4 \end{cases} \quad \mathbf{c}_i = \begin{cases} (0,0) & i = 0\\ (\pm 1,0), (0,\pm 1) & i = 1:4 \end{cases}$$
 (20)

The weighting factors are chosen such that the moments of the thermal distribution function are conserved during the streaming and collision steps of the DD-TLBM model.

Utilizing the Chapman-Enskog expansion method, it is possible to derive the continuum energy equation corresponding to the thermal distribution function in the form of

$$\frac{\partial T(\mathbf{r},t)}{\partial t} + \mathbf{u}_{\text{real}} \cdot \nabla T(\mathbf{r},t) = \nabla \cdot (\alpha \nabla T(\mathbf{r},t)) + \varepsilon + G^{\text{ext}} - T(\mathbf{r},t) \nabla \cdot \mathbf{u}_{\text{real}}.$$
(21)

In the above relation, the thermal diffusivity is denoted as α , and ϵ is an unwanted term that arises due to the presence of the force term in

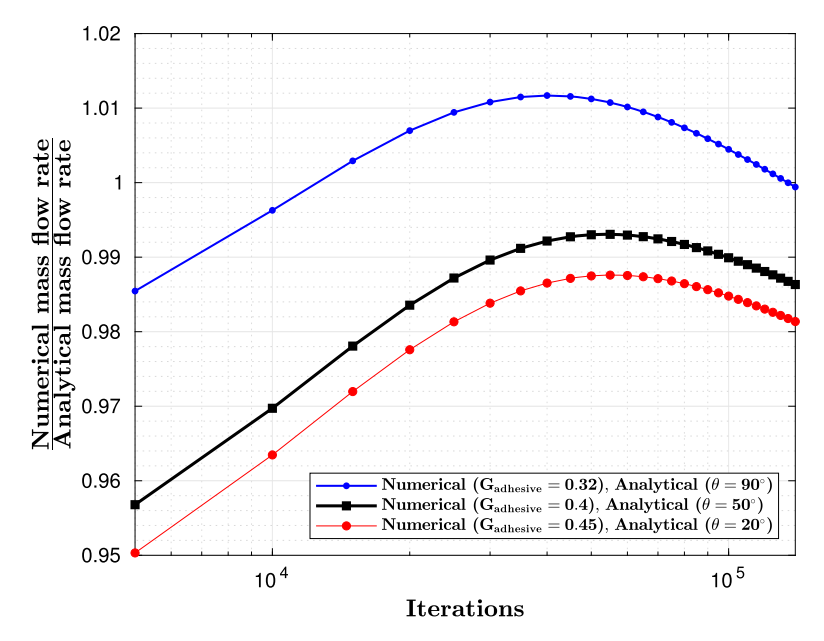


Fig. 3. Comparison between numerical simulation and analytical model regarding the evaporation of a fluid in a nanochannel.

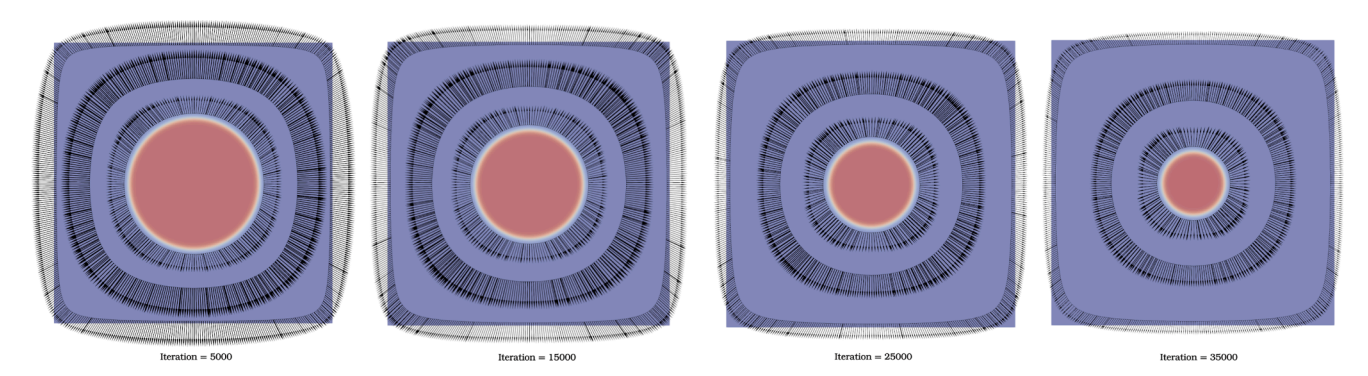


Fig. 4. Visualization of a droplet evaporating at constant pressure for different iterations. Velocity vectors are drawn along lines of constant temperature.

Eq. (9) (Zarghami and Van den Akker, 2017),

$$\varepsilon = (\frac{1}{2\tau_g} - 1)\omega_i^T c_v T(\mathbf{r}, t) \frac{\mathbf{c}_i \cdot \mathbf{F}(\mathbf{r}, t)}{c_s^2},$$
(22)

where c_{ν} stands for specific heat capacity at constant volume. However, the macroscopic thermal energy equation reads

$$\rho c_p \frac{\partial T}{\partial t} + \rho c_p \mathbf{u}_{\mathrm{real}} \cdot \nabla T = \nabla \cdot (k \nabla T) + \tau_{i,j} \frac{\partial u_i}{\partial x_j} - \frac{T}{v} \left(\frac{\partial v}{\partial T} \right)_p \frac{DP}{Dt} + Q^{\prime\prime\prime}. \tag{23} \label{eq:23}$$

In the above relation $\tau_{i,j}$ and Q''' stand for the force per unit area acting on a surface (stress) and the heat sink or source per unit volume, respectively. The continuum equation, Eq. (21), reproduces the balance equation for thermal energy if dissipation and the pressure term, the second and third term of the RHS of Eq. (23), respectively, can be neglected. These conditions are met for the flow of liquid, but to reproduce the Joule-Thomson effect for the adiabatic flow with friction through a duct, both the dissipation and the pressure terms in Eq. (23) must be concluded.

The term that accounts for phase change is referred to as σ , and it can be defined as follows Zarghami and Van den Akker (2017):

$$\sigma = \rho h_h i \phi'(\rho) \frac{\mathrm{d}\rho}{\mathrm{d}t},\tag{24}$$

where h_{ϕ} represents the enthalpy associated with a phase change process (e.g., enthalpy of vaporization). The marker function $\phi(\rho)$ is defined based on the density of the fluid. This function takes a value of zero in the vapor phase and one in the liquid phase and increases linearly with

density for values in between,

$$\phi(\rho) = \frac{\rho - \rho_{\text{vap}}}{\rho_{\text{liq}} - \rho_{\text{vap}}}.$$
 (25)

The term σ can be considered as the amount of heat per unit volume supplied from external sources ($\sigma = Q'''$).

Finally, the energy conservation relation for multiphase flows with phase change at the macroscopic level can be represented as follows:

$$\frac{\partial T}{\partial t} + \mathbf{u}_{\text{real}} \cdot \nabla T = \frac{\nabla \cdot k \nabla T}{\rho c_p} + \frac{\sigma}{\rho c_p}.$$
 (26)

When comparing Eq. (26) with Eq. (21), one can observe that Eq. (21) has unwanted components that must be adjusted to replicate the macroscopic energy (Eq. (26)). Consequently, the external source term in Eq. (18) is specified as a correction (Zarghami and Van den Akker, 2017), which is given by

$$G^{\text{ext}} = T \nabla \cdot \mathbf{u}_{\text{real}} - \nabla \cdot (\alpha \nabla T) + \frac{\nabla \cdot k \nabla T}{\rho c_p} + \frac{\sigma}{c_p} - \varepsilon.$$
 (27)

The liquid-vapor interface properties η (such as thermal diffusivity) are calculated by:

$$\eta = [1 - \phi(\rho)]\eta_{\text{vap}} + \phi(\rho)\eta_{\text{liq}}.$$
 (28)

By using this equation, the properties of the interface change monotonically within the interface region. This means that they change gradually and consistently in a specific direction. This equation allows for the calculation of various properties of the interface, indicating

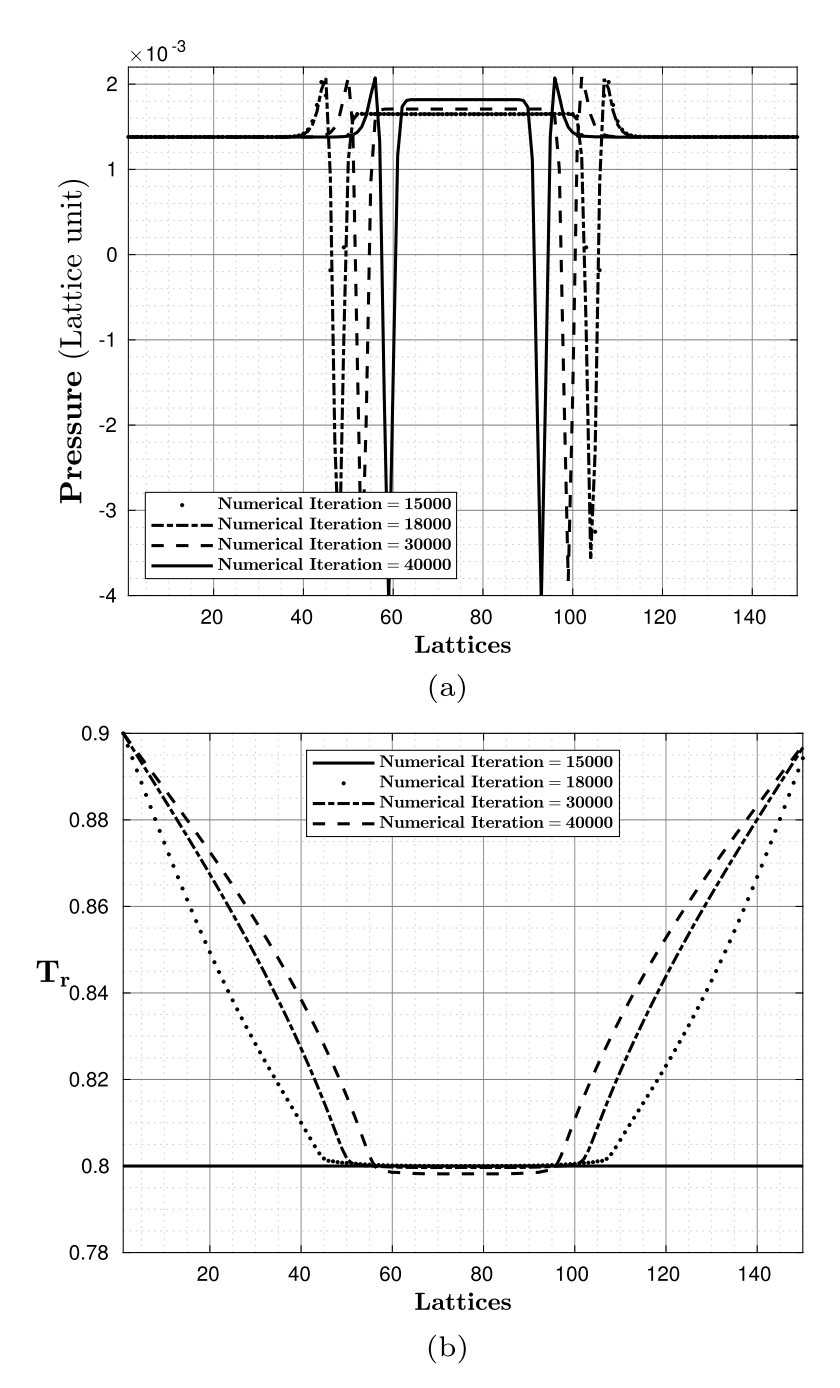


Fig. 5. a) Pressure, b) Temperature distribution along the centerline at different times.

that the properties of the interface vary smoothly and continuously within the interface region. Unless otherwise noted, the simulations utilize the following values for the thermal diffusivities and specific heats of the liquid and vapor: $\alpha_{\rm liquid}=10^{-3}$, $\alpha_{\rm vapor}=10^{-2}$, $c_{\rm p,liquid}=5.1$, and $c_{\rm p,vapor}=2.50$ (Zarghami and Van den Akker, 2017). The kinematic viscosity of the liquid and the vapor are defined as $v_{\rm liq}=c_s^2\left(\tau_{liq}-\frac{\Delta t}{2}\right)$ and $v_{\rm vap}=c_s^2\left(\tau_{vap}-\frac{\Delta t}{2}\right)$, respectively. Our model's working fluid is carbon dioxide at a reduced temperature around $T_r\approx 0.8$ ($T\approx 243~K$). By choosing the relaxations for the vapor and the liquid to be $\tau_{vap}=1$ and $\tau_{liq}=0.75$, respectively, the viscosity ratio is $v_{\rm vap}/v_{\rm liq}=2$, which is close to the physical ratio. The density ratio is controlled by the value of the domain temperature and pressure through the equation of state, and for the temperature and pressure range studied in our work, this ratio is around 40.

The same discrete distribution without external parameters is considered the governing equation for the solid nodes. Since the velocity of the solid nodes is zero, conduction is the only heat transfer mechanism. In this study, we assumed that the thermal conductivity of the solid nodes is 50 times that of the liquid phase.

2.2. Determining the domain, boundary conditions, and initialization

This section describes the domain geometry, initial condition, and boundary conditions. A two-dimensional domain with a size of $N_x \times N_y = 32 \times 800$ lattices is used to describe a nanoslit. As shown in Fig. 1a, small inlet and outlet bulk regions are utilized to prescribe the inlet and outlet boundary conditions to the slit. In these bulk regions, periodic boundary conditions are applied in the transversal direction. From x=20 to 780, the domain is restricted with walls that have changeable

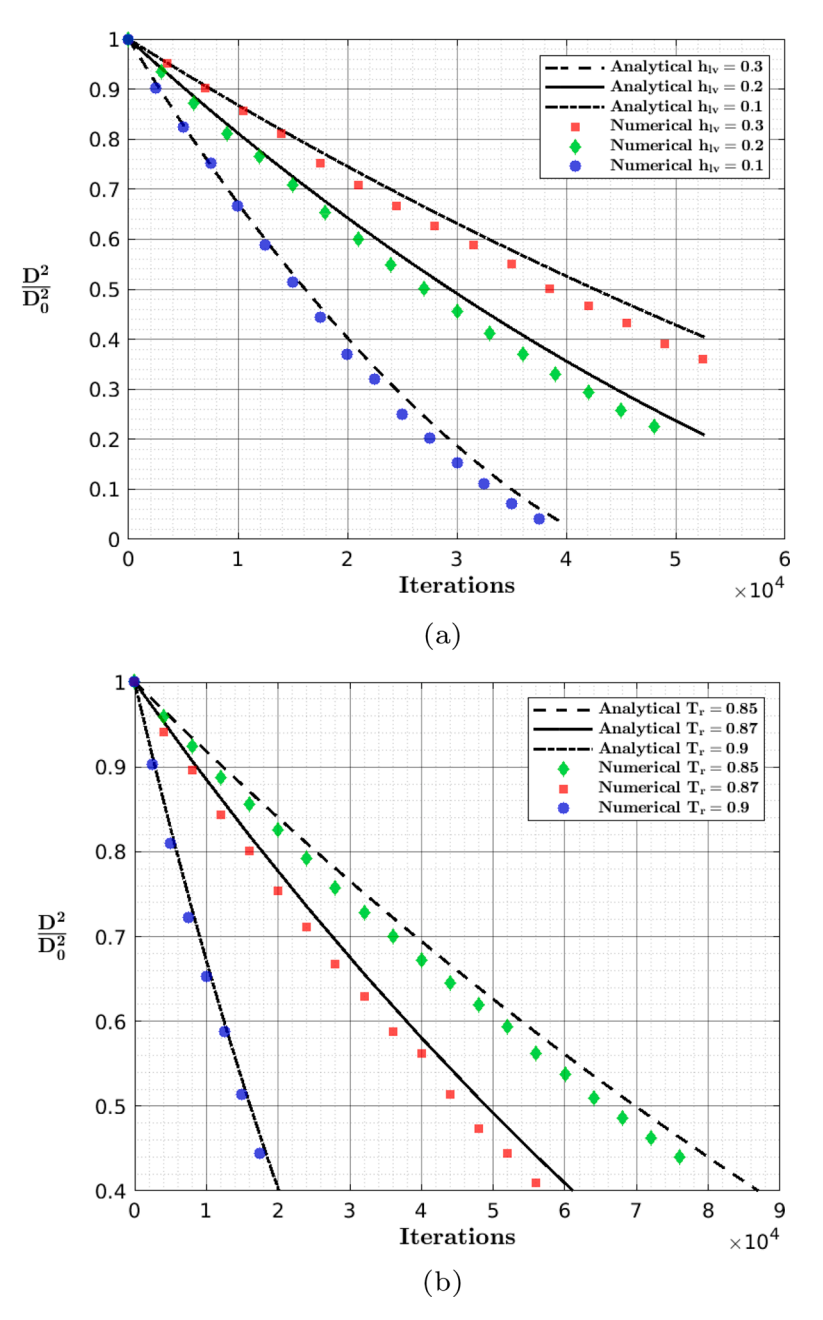


Fig. 6. Comparison between the simulation and D² law for (a) different enthalpies of vaporization at the boundarily temperature $T_r = 0.9$ and (b) different boundary temperatures with $h_{lv} = 0.1$.

thicknesses to consider the effect of nanoslit width. The halfway bounce-back boundary condition is employed for solid nodes next to fluid nodes, which stands for a nonslip boundary on the macroscopic scale. By combining this boundary with the halfway specular boundary condition, one can add the effect of slip on the wall (Succi, 2002). Regarding the initialization, essentially the slit, i.e., the sub-domain located between x = 20 and x = 780, was initialized as liquid while the rest was initialized as gas nodes. At the interface, the densities were smoothed out (Huang et al., 2011).

$$\rho(x,y) = \rho_g + \frac{\rho_l - \rho_g}{2} \times \text{abs} \left\{ \tanh \left[\frac{2(x-20)}{W} \right] - \tanh \left[\frac{2(x-780)}{W} \right] \right\}. \tag{29}$$

In the above relation, ρ_l and ρ_g are the initial gas and liquid densities from Maxwell construction, and W is the width of the initial interface,

which is equal to 5. After initialization, a constant temperature was prescribed for the entire domain. After 50,000 iterations, isothermal equilibrium was reached, see Fig. 1b. It is worth mentioning that the equilibrium pressure of the gaseous side is regarded as the capillary pressure. Consequently, the nonequilibrium extrapolation scheme is applied to the inlet and outlet boundaries to provide the constant pressure as the boundary conditions . In this regard, to maintain a constant inlet and outlet bulk pressure, the Neumann boundary condition is employed on the velocity to estimate the undetermined distributions of f_i at the inlet and outlet boundaries. Next, a new equilibrium distribution function, $f_{i,new}^{eq}$, is calculated by the C-S EOS for the local lattices to achieve the desired density taking into account the initial pressure and current temperature. At the outlet, the temperature from which the density is calculated is either set equal to the upstream temperature for the diabatic description or is determined from the Joule-Thomson coefficient

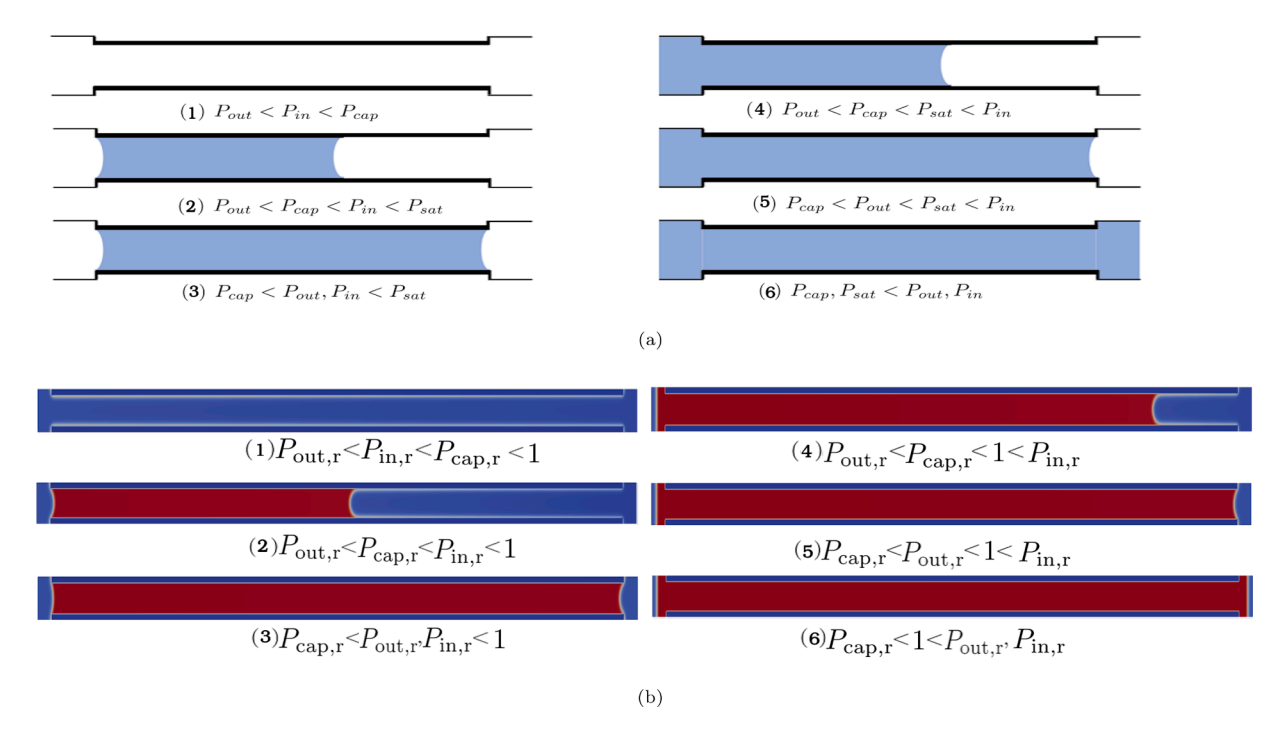


Fig. 7. Visual representations demonstrating fluid density within a nanopore under different equilibrium and nonequilibrium states. a) Fluid distribution according to Lee and Hwang (1986). Adapted with permission from Rathi et al., Langmuir 35, 5702 (2019). Copyright 2019 American Chemical Society. b) Present work.

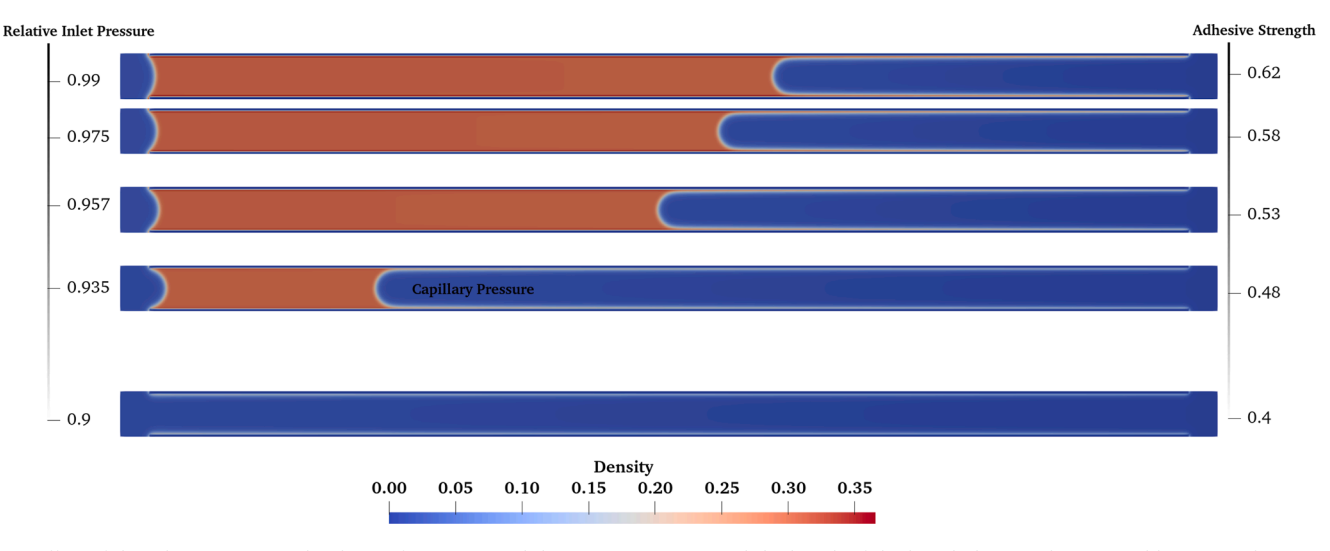


Fig. 8. Effect of the inlet pressure on the shape of upstream and downstream menisci and the length of the liquid phase at the nonequilibrium steady states for $p_{\text{out.r}} = 0.37$. The range of adhesive strength is shown on the left.

for the adiabatic description. Lastly, the unknown distribution functions are calculated as follows Fei et al. (2022):

$$f_i^{unknown} = f_i + f_{i,new}^{eq} - f_i^{eq}, \tag{30}$$

where f_i^{eq} is the equilibrium distribution corresponding to the undetermined directions of the boundary nodes.

Regarding the thermal boundary conditions, the adiabatic boundary is considered for the solid nodes restricting the domain to prevent heat transfer in the perpendicular direction. Concerning the thermal boundary condition for the exit nodes, based on the adiabatic prediction, the Neumann thermal boundary condition is applied to avoid heat transfer. For the diabatic description, the temperature at the outlet is specified and adjusted to match the upstream temperature at negative infinity (Loimer et al., 2011). From applying the energy equation upstream of

the slit (Loimer et al., 2019), for both descriptions, an exponential function is introduced to describe the temperature boundary layer preceding the nanoslit from negative infinity to the entrance of the nanoslit. For the solid nodes, a constant thermal conductivity that is 20 times higher than that of the liquid nodes is assumed. Furthermore, to provide the nonequilibrium steady state condition, 1,500,000 iterations were carried out for each simulation.

2.3. Conversion between lattice units and physical units

From dimensional analysis, in order to convert four basic quantities (mass, length, time, temperature) from lattice units to physical units, relations for four independent quantities must be used. In this study, the C-S EOS is used, which contains the parameters $a_{\rm Ph}$, $b_{\rm Ph}$ and the

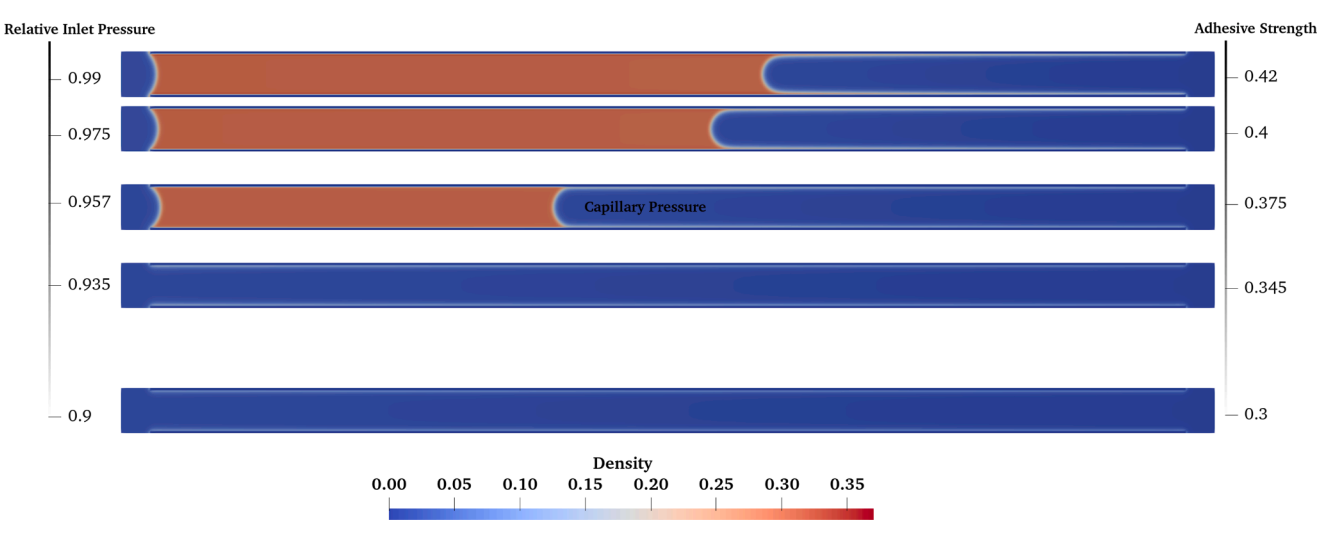


Fig. 9. Effect of the inlet pressure on the shape of upstream and downstream menisci and the length of the liquid phase (location of the menisci) at the nonequilibrium steady states for $p_{out,r} = 0.37$. The range of adhesive strength is shown on the right.

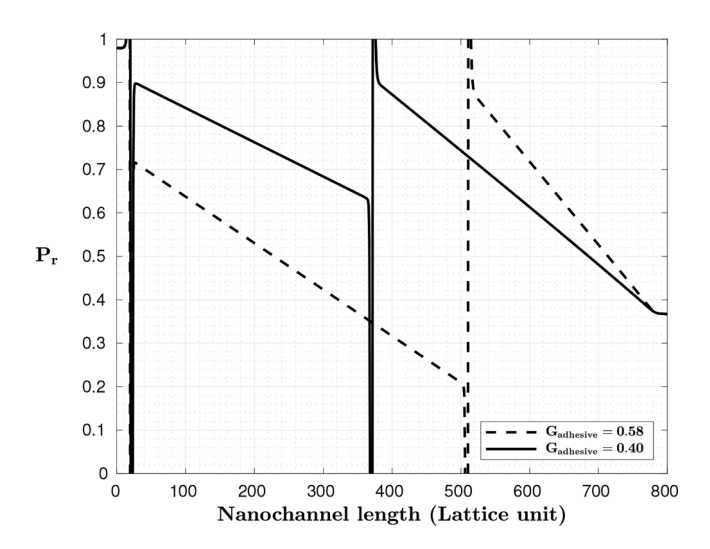


Fig. 10. Pressure variation along the center line from upstream to downstream for $G_{\rm adhesive}=0.58$ and $G_{\rm adhesive}=0.40$ at the relative inlet pressure $p_{\rm in,r}=0.98$ and the relative outlet pressure $p_{\rm out,r}=0.37$.

specific gas constant $R_{\rm Ph}$. However for the C-S EOS, the critical pressure $p_{\rm c,Ph}$, the critical temperature $T_{\rm c,Ph}$ and $R_{\rm Ph}$ are related to $a_{\rm Ph}$ and $b_{\rm Ph}$ by

$$a_{\rm Ph} = \frac{0.4963 R^2 T_{\rm c,Ph}^2}{p_{\rm c,Ph}}, \ b_{\rm Ph} = \frac{0.1873 R T_{\rm c,Ph}}{p_{\rm c,Ph}}.$$
 (31)

While in lattice units, a, b, and R are chosen arbitrarily to be 1, 4, and 1, respectively. Hence, from the connections of a, b, and R between physical and lattice units, we have three equations. The fourth is provided by the surface tension. For instance, taking carbon dioxide as the working fluid with physical properties equal to $T_{\rm c,Ph}=304.1282~K$, $p_{\rm c,Ph}=7.3773~MPa$ and $R_{\rm c,Ph}=0.18892~Jg^{-1}K^{-1}$ and following the procedure for unit conversion, see e.g. (Wang et al., 2022), the conversion coefficients between lattice length and physical length for different domain temperatures are presented in Table 1. As can be seen in Table 1, one lattice extends over less than one nm, hence one lattice may contain only two or three molecules of carbon dioxide in a dense packing. Since the lattice-Boltzmann method can be regarded as continuum description, the lattice spacing can be seen as the resolution of the continuum solution. However, with respect to the approximation of the adhesive

Table 1Lattice unit-physical length conversion coefficients at different temperatures for carbon dioxide as the working fluid.

$T_{\rm r}$	$T_{\mathrm{domain}}(K)$	$\sigma_{\rm ph}(N/m)$	$\sigma_{\mathrm{LBM}}(lattice\ unit)$	$LP_{\rm l}(nm/lattice)$
0.7	212.88 243.30	0.0173 0.01047	0.0159 0.00815	0.652 0.770
0.9	273.71	0.0043839	0.00312	0.842

force, F^{adhesive}, the lattice spacing corresponds to the physical reach of the adhesive force between the wall and fluid particles.

3. Validation

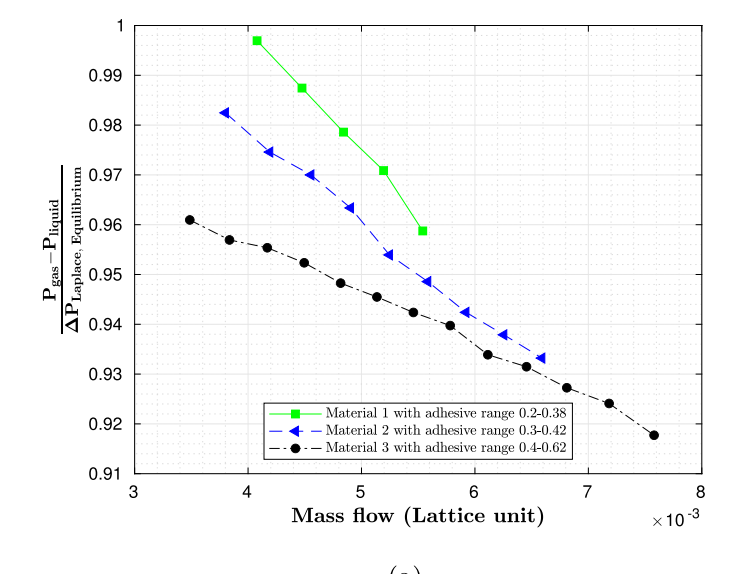
3.1. Evaporation from a capillary tube due to a pressure reduction

In order to verify the accuracy of the current numerical model for quasi-isothermal evaporation caused by pressure differences, we conducted a simulation of evaporation in a capillary nanotube and compared the outcomes to an analytical solution when the vapor mass flow rate is restricted by viscous friction, cf. Cueto-Felgueroso et al. (2018).

The simulated nanotube has a length of 800 lattices and a width of 32 lattices, with the left side being open for evaporation, as shown in Fig. 2. According to the analytical model, the diffusive scaling of the evaporative flux over time is expressed as $\dot{m}(t) = (0.5 D_{\nu} (\rho_{\nu}^{\rm meniscus} - \rho_{\nu}^{\rm out})/(\rho_{1}^{\rm meniscus} - \rho_{\nu}^{\rm meniscus}))^{0.5} t^{-0.5}$, where $\rho_{1}^{\rm meniscus}$, and $\rho_{\nu}^{\rm out}$ are the liquid density, vapor density at the meniscus, and the vapor density at the outlet boundary, respectively. The densities of transition, $\rho_{\nu}^{\rm meniscus}$ and $\rho_{1}^{\rm meniscus}$, are derived from density profiles that are measured along the channel axis using the Lattice unit. The diffusivity D_{ν} is defined as follows:

$$D_{v} = \frac{\rho_{r}^{2}}{\mu_{r}} \left[-6 + \frac{8T_{r}}{3(3 - \rho_{r})} \left(\frac{3}{\rho_{r}} - \frac{3}{3 - \rho_{r}} \right) \right]. \tag{32}$$

Regarding the numerical simulation, first, the capillary is filled with liquid at a reduced temperature of $T_r = 0.8$. Once the system is in equilibrium, the pressure at the left boundary is reduced to 0.36 times the equilibrium gas pressure. Here, for the simulation of carbon dioxide, $T_r = 0.8$ corresponds to T = 243.3~K, the saturation pressure $p_{\rm sat} = 1.52~MPa$, and the equilibrium pressure $p_{\rm eq} = 1.4~MPa$. For iteration 100,000 of Fig. 2, the density and the kinematic viscosity of the liquid are $1217~kg/m^3$ and $5.13 \times 10^{-8}~m^2/s$, respectively. The density and the kinematic viscosity of the gaseous phase at the left boundary are



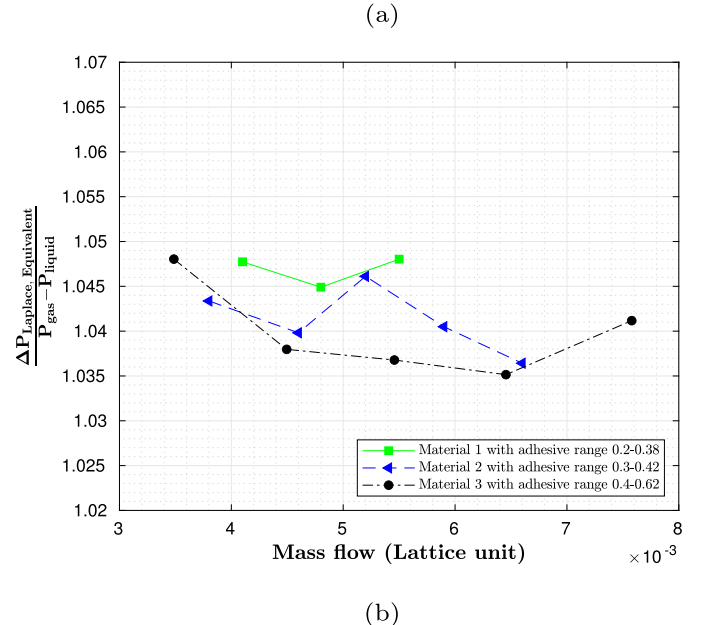


Fig. 11. Effect of the mass flow rate on the pressure difference across the downstream meniscus for different materials with different range of adhesive strengths with $p_{\text{out},r}=0.37$. a) With respect to $2\sigma/(\text{radius})$ of curvature at equilibrium), b) With respect to $2\sigma/(\text{measured radius})$ of curvature at nonequilibrium).

 $27.48 \frac{Kg}{m^3}$ and $1.026 \times 10^{-7} \ m^2/s$, respectively. We examined different contact angles, indicated by various adhesive force strengths, for the solid walls. The relationship between mass flow rate and time is plotted using the variables in the lattice unit for the analytical model. As shown in Fig. 3, our simulation results match the analytical solution reasonably well. However, there is a higher deviation between the simulation and analytical results for the first few iterations and stronger adhesive strength. The larger deviation is probably due to the larger deviation of the velocity profiles from the parabolic shape in the shorter gas-filled region, as can be seen at the top of Fig. 2. The derivation of Eq. (32) is based on the assumption of a parabolic velocity profile throughout the entire gas-filled region. Only for a long enough gas flow section is this assumption valid.

3.2. Evaporation of a droplet due to a temperature difference

The analytically traceable evaporation of a droplet into a gaseous environment is reproduced to validate the simulation of the phase change

process caused by a temperature difference. To do this, a droplet with 35 lattice radius is used in the center of a domain with a mesh size of 150×150 for the simulation. Once the droplet reaches equilibrium at $T_r = 0.8$, the temperature of the boundaries is increased, creating a temperature difference that causes evaporation. Fig. 4 shows the colorcoded density field of an evaporating droplet at four instances in time. Velocity vectors are drawn in the figure along lines of constant temperature. The specific arrangement and implementation details of the D2Q9 LBM setup could lead to a velocity field that is not perfectly radial, as can be seen in Fig. 4. Close to the droplet the velocity vectors pointing to the corners seem to be larger than the velocity vectors normal to the boundary. Close to the boundary, the tendency in the velocity distribution seems to be reverse, see the leftmost and the rightmost images in Fig. 4. Also, the temperature distribution is not completely radially symmetric, see the isotherms in Fig. 4. Such imperfections have also been observed in other computations of an evaporating droplet (Albernaz et al., 2015; Zarghami and Van den Akker, 2017; Fei et al., 2022). To address the possible cause of the imperfections seen in Fig. 4, we have conducted further investigations, including an analysis of boundary conditions and a revision of our discretization scheme for the energy equation. These additional studies are detailed in the Supporting Information and suggest that the anisotropy in the radially symmetric problem stems from the discretization scheme used for energy equation.

The D^2 law provides an analytical solution for droplet evaporation caused solely by diffusion based on Eq. (33). According to this analytical prediction, the droplet temperature and the vapor pressure must remain constant during evaporation. As the temperature at the boundaries increases, the vapor is heated and results in diffusion-driven evaporation,

$$D_{\rm drop}^2 \left[\frac{1}{2} + \ln \frac{L_{\rm d}}{D_{\rm drop}} \right] = D_{\rm init}^2 \left[\frac{1}{2} + \ln \frac{L_{\rm d}}{D_{\rm init}} \right] - \frac{8\alpha_{\rm i}\rho_{\rm i}t}{\rho_{\rm liquid}} \ln(1 + Sp). \tag{33}$$

In the given equation, $L_{\rm d}$ represents the length of the domain, $D_{\rm drop}$ is the diameter at a specific instant, and the subscript i refers to the interface. Additionally, Sp is a non-dimensional parameter known as the Spalding number, $Sp = C_p(T_{\rm boundary} - T_{\rm drop})/h_{\rm lv}$, where $h_{\rm lv}$ is the specific enthalpy of vaporization. The center line's pressure and temperature distributions for different time steps with the boundary condition described earlier are illustrated in Fig. 5. Fig. 5a reveals that, despite the bulk regions' constant pressure during evaporation, there are pressure variations across the interface. This suggests that the mechanical stability condition is not met around the interface. This issue occurs in the lattice Boltzmann methods when a force is applied to introduce the nonideal EOS. An important observation from the simulations is that the droplet's pressure increases as the iterations progresses due to the Young-Laplace equation and the decreasing radius with time. Since the temperature of the droplet stays constant, the surface tension does not change. Therefore, a decrease in the droplet's radius causes an increase in the pressure inside the droplet. Additionally, Fig. 5b displays the temperature distributions at various times. It is apparent that the droplet's temperature remains constant during the evaporation process. Figs. 6a and b exhibit the time-dependent behavior of the droplet's normalized squared diameter under different temperatures of the domain boundaries and various latent heat values. The numerical outcomes are compared with the D^2 law, and the findings demonstrate good agreement.

Fig. 6b depicts the findings obtained at different temperatures of the domain boundaries for $h_{\rm lv}=0.1$. The graph reveals that an increase in the surrounding temperature results in faster evaporation of the droplet. Fig. 6a illustrates a comparison between the numerical results and the D_2 law at a surrounding temperature of $T_r=0.9$ and various latent heats. The data demonstrate that an increase of the enthalpy of vaporization leads to a decrease in the rate of evaporation since more energy is required to transform the liquid into vapor.

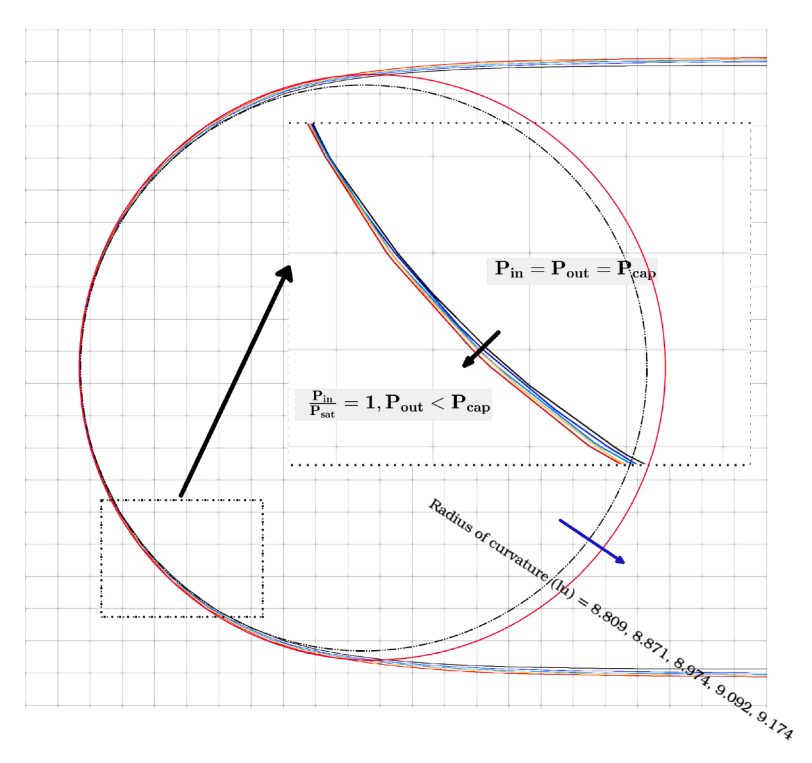


Fig. 12. Contours of the downstream interface for the material with the range of adhesive strength $G_{\text{adhesive}} = 0.4 - 0.62$ and $p_{\text{out,r}} = 0.37$. With increasing upstream pressure, the radius of curvature of the meniscus increases (solid lines). The dash-dotted line indicates the radius of curvature for stationary state ($p_{\text{out}} = p_{\text{in}} = p_{\text{cap}}$).

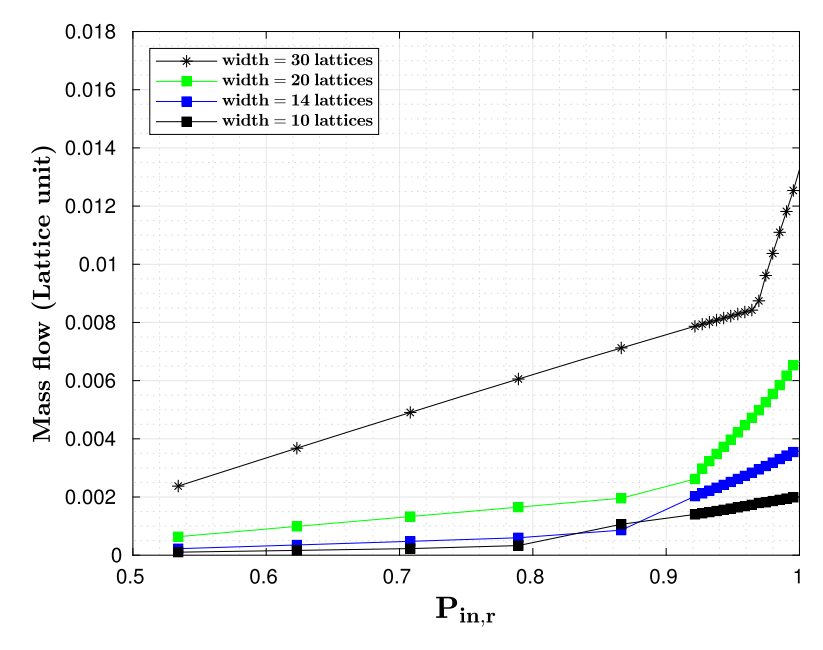


Fig. 13. Influence of the nano-slit pore width on the mass flow rate for the solid material with the adhesive range $G_{\text{adhesive}} = 0.4 - 0.62$ and the relative outlet pressure $p_{\text{out,r}} = 0.37$.

3.3. Steady state nonequilibrium phase distribution inside a nanopore for different bulk conditions

Efforts have been made to link experimentally measurable quantities such as mass flow rate, pressure, and nanoporous structure to the bulk conditions of the media endpoints via the transport models (Choi et al., 2001). Lee and Hwang (1986) tried to depict the possible states (illustrated in Fig. 7a) through a combination of continuum models. They

assumed that a group of parallel cylindrical capillaries could represent the porous structure and employed the Knudsen diffusion model for gas flow. Darcy's model for flow through porous media was used to simulate the flow of condensate, which reduces to the Hagen-Poiseuille model if a group of cylindrical capillaries represents the porous medium, and Gilliland's hydrodynamic flow model was used to simulate the surface flow. Our model used the same range of bulk pressure boundary conditions regarding the saturation and capillary pressures as the reference

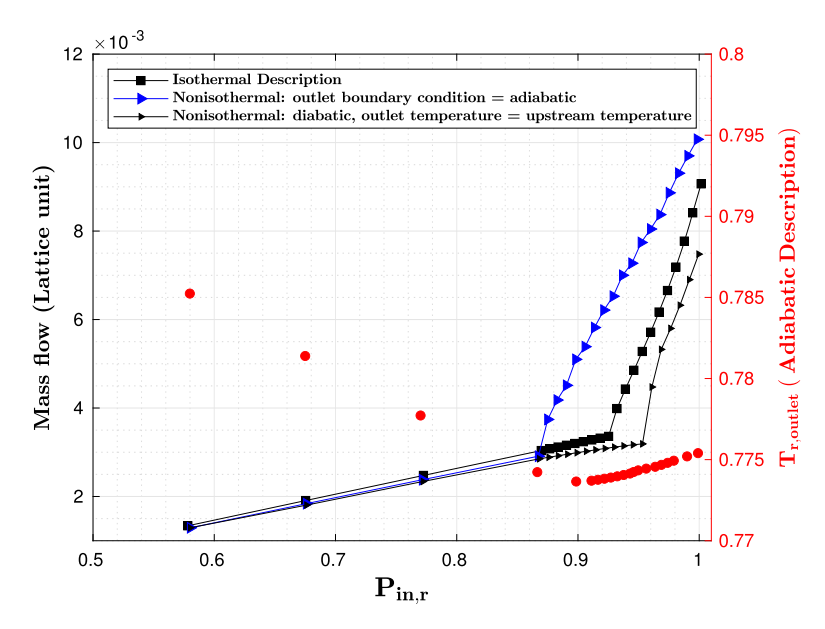


Fig. 14. Effect of the temperature field on the mass flow rate for the for the solid material with the adhesive range $G_{\text{adhesive}} = 0.4 - 0.62$ and the relative outlet pressure $p_{\text{out},r} = 0.37$.

points to represent different states. In this regard, we introduce the relative pressure, which is described as $p_{\rm r}=p/p_{\rm sat}$ for the relative capillary pressure, relative inlet and outlet bulk pressures. As can be observed in Fig. 7b, the density distribution is the same for all situations compared to the study by Lee and Hwang (1986). Moreover, investigation on phase equilibrium of methane in nanopores under the effect of adsorption by Huang et al. (2021) indicates that mesopores are entirely filled once the vapor starts to nucleate at sufficiently high relative vapor pressures of pure fluid. This result is comparable with the case illustrated in Fig. 7b(3) and a(3), where $p_{\rm in,r}$ equals $p_{\rm out,r}$.

4. Result and discussion

4.1. The effect of the nanopore width on the mass flow rate; isothermal consideration

During the transient simulation, the liquid-vapor interface progressively develops and ultimately stabilizes under the influence of the inlet and outlet pressure boundary conditions, leading either to a steady interface configuration or to a purely gas-phase flow. The pressure difference between the upstream and the downstream menisci is responsible for the increase in mass flow during capillary condensation. In a case where the inlet and outlet bulk pressures are the same and greater than the capillary pressure, the radii of curvature of both menisci are equal, hence, the pressure difference across both menisci are the same. However, as shown in Figs. 8 and 9 which represent the flow through slits made of different solid materials, when the relative inlet bulk pressure $p_{\rm in \, r}$ approaches one while the relative outlet pressure remains constant with $p_{\text{out r}} = 0.37$, the radius of curvature of the upstream meniscus increases significantly compared to that of the downstream meniscus. Consequently, the pressure difference across the downstream meniscus becomes much greater than the pressure difference across the upstream meniscus, resulting in a substantial additional pressure difference that increases the mass flow rate. For the solid material with larger range of adhesive strength (Fig. 8), the effect of capillary condensation on the mass flow rate increase occurs for a smaller relative inlet pressure compared to that with smaller range of adhesive strength (Fig. 9). Additionally, the solid material with the larger adhesive strength range causes the downstream menisci radius to be smaller, which can be related to the length of the liquid phase at the steady state.

Fig. 10 displays the pressure variation along the centerline from the upstream to downstream for the relative inlet pressure $p_{\rm in,r}=0.98$. For the solid surface with $G_{\rm adhesive}=0.58$, the density and the kinematic viscosity of liquid is $1177~kg/m^3$ and $5.13\times 10^{-8}~m^2/s$, respectively. The density of the gas varies between $78.5~kg/m^3$ close to the meniscus at the pressure P=1.3376~MPa and $27.48~kg/m^3$ at the pressure P=.5624~MPa for the outlet. The kinematic viscosity of the gas remains approximately constant and is $1.026\times 10^{-7}~m^2/s$. The pressure difference across the downstream meniscus for the larger adhesive strength is significantly greater than the case with smaller adhesive strength, which is consistent with the size of the meniscus curvature. As soon as steady state is achieved, i.e., there is a constant mass flow rate throughout the channel, the menisci stay fixed and maintain their shape.

Fig. 11a displays the numerically obtained pressure difference across the downstream meniscus with respect to the equilibrium pressure difference for the equilibrium contact angle. There is a two-phase flow inside the nanoslit, i.e., the flow configuration is that depicted in Fig. 7b(2). At the equilibrium state, there is a relation between the adhesive strength and the contact angle (Sodagar-Abardeh et al., 2023), and one can measure the contact angle by having the value of the adhesive strength. Consequently, the equilibrium pressure difference along the downstream interface can be calculated with the Young-Laplace relation $\Delta p = \sigma \cos \theta / \text{slit}$ width. Fig. 11a shows two effects. One, when the mass flow rate is zero, i.e., for a stationary two-phase state in a nanochannel, the pressure difference across the meniscus obtained numerically is smaller than the Young-Laplace pressure $\Delta p_{\text{Laplace}}$. With increasing the adhesive strength, i.e., decreasing contact angle and decreasing radius of curvature, the deviation increases (Sodagar-Abardeh et al., 2023). The second effect shown by Fig. 11a is the decrease of pressure difference ratio with increasing mass flow rate. Fig. 11a also shows the pressure difference ratio is close to 1 for the solid material with the smaller range of adhesive strength $G_{\text{adhesive}} = 0.2 - 0.38$, the green square, while this ratio is below 0.96 for the material with the higher range of adhesive strength $G_{\rm adhesive} = 0.4 - 0.62$, the black circle. The pressure difference determined numerically could decrease with increasing mass flow rate either because the Young-Laplace's equation is not obeyed, or because the interface is deformed. In simulations of two-phase flow, accurately representing the interface is crucial. One useful characteristic of the current model, which is a type of diffusiveinterface model, is its capability to automatically adapt the interface between the two phases and calculate the curvature of the interface, as

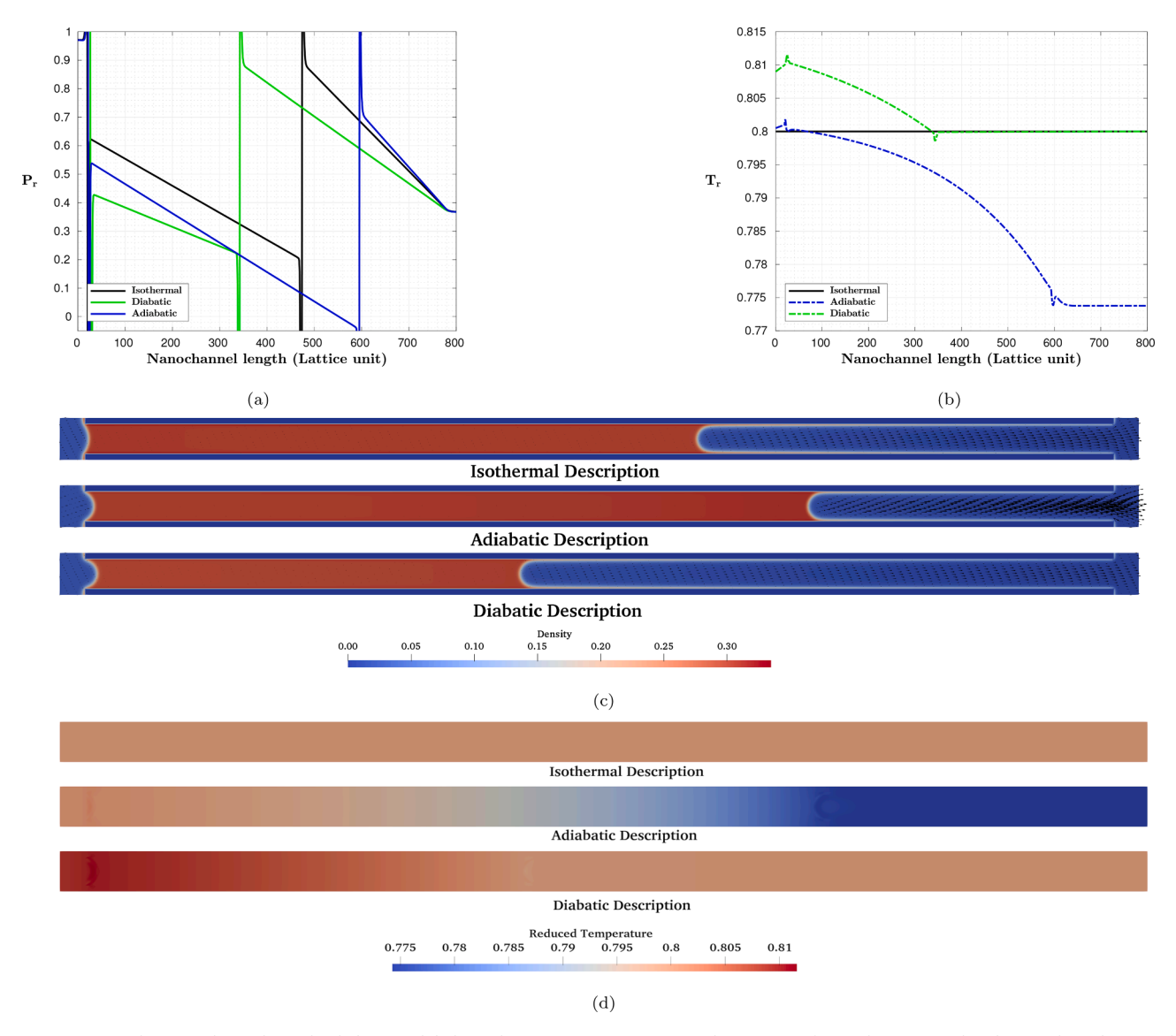


Fig. 15. Comparison between the isothermal, adiabatic and diabatic descriptions at $p_{\text{in,r}} = 0.97$ and $p_{\text{out,r}} = 0.37$ for: a) the pressure distribution along the centerline, b) the temperature distribution along the centerline, and c) the density contours and the meniscus shapes, d) the temperature fields.

illustrated in Fig. 12. To test the reasons for the change in pressure difference ratio, the shapes of the interfaces (from the numerical simulation) were traced, see Fig. 12. After determining the coordinations of points along an interface, the circle that best fits the points is determined using the least square method. Subsequently, the radius of curvatures is obtained, and the Young-Laplace equation can be evaluated with these curvatures, $\Delta p_{\rm Laplace,equivalent}$. Fig. 11b plots the ratio of the numerically obtained pressure difference to $\Delta p_{\rm Laplace,equivalent}$, the pressure difference according to the shape of the meniscus. The ratio is very close to one in all the cases, and it is independent of the mass flow rate and the contact angle. It only shows a small noise about its approximate contact value of 1.045. Hence, increasing mass-transfer deforms the meniscus and Young-Laplace's equation remains valid.

The capillary pressure is one of the criteria used to describe the nonequilibrium steady state condition (Fig. 7b). Following our previous work (Sodagar-Abardeh et al., 2023), to estimate the equilibrium gas pressure of a curved interface, which represents capillary pressure in this study, one should consider the effect of the inlet bulk pressure, the chemical features of the solid material, the nanochannel width, and the domain temperature. For the two-dimensional isothermal description, by changing the width of the nanopore, the value of the capil-

lary pressure changes. By comparing Figs. 8 and 9, it is evident the chemical features of a solid material significantly influence both the beginning of capillary condensation and the steady-state liquid length within the nanopore. Fig. 13 illustrates how the mass flow rate is affected by changes in the width of a nanoslit. If the width of the nanoslit increases, the mass flow rate will also increase when the inlet pressure is far less than the saturation pressure. Additionally, the incline of the line displaying the relationship between mass flow rate and pressure ratio becomes steeper with increasing the slit width, suggesting a more significant contribution from the viscous flow. Our previous research (Sodagar-Abardeh et al., 2023) has demonstrated that an increase in nanopore diameter results in a shift of the capillary pressure toward the saturation bulk pressure. As a result, the relative inlet pressure value required for capillary condensation to occur increases for larger pore sizes. This shifts the kink point toward one for nanoslit with larger width. For example the minimum relative inlet pressure for the slit with 30 lattices width to experience capillary condensation is about $p_{\text{in,r}} = 0.96$, while this value for the case with 20 lattices width is about $p_{in.r} = 0.92$. Capillary pressure causes higher pressure difference at the downstream meniscus in nanopores with a smaller diameter. This can explain why for the same range of relative inlet pressures, the mass flow rate through a

smaller nanopore is greater than ones with a larger diameter. In Fig. 13, there is a range of relative inlet pressure between 0.84 and 0.88 where the mass flow rate of a nanoslit with ten lattices width is higher than that with 14 lattices width.

4.2. Effect of the temperature field on the mass flow rate

After considering the influences of different parameters on the mass flow rate for the isothermal prediction, this section investigates the effect of the outlet temperature reduction and the temperature boundary layer on the mass flow rate. For the adiabatic downstream boundary condition, i.e., $(\partial T/\partial x)_{\text{outlet}}=0$, the outlet temperature is determined from integrating the Joule-Thomson coefficient μ_{JT} of a specific substance,

$$T_{\text{inlet}}^{\text{LBM}} - T_{\text{outlet}}^{\text{LBM}} = \int_{p_1}^{p_2} \mu_{JT}^{\text{LBM}} dP^{\text{LBM}}.$$
 (34)

Determining the outlet temperature makes it possible to calculate the temperature-dependent properties at the outlet. The outlet temperature is always lower than the inlet temperature when a vapor flows through a porous membrane because the Joule-Thomson coefficient for vapors, i.e., for a gaseous phase below the critical temperature, is always positive. By determining the temperature of the downstream side with the mentioned procedure (see Fig. 14), after reaching the steady state for the equilibrium calculation (considering the periodic boundaries for inlet and outlet and isothermal condition), the energy population is coupled with the density distribution function to evaluate the effect of the temperature reduction on the mass flow rate in the adiabatic description. Zou and He (1997) boundary conditions are employed to implement the fixed temperature and heat flux boundary conditions. Furthermore, the adiabatic condition is considered for the walls restricting the domain as the thermal boundary conditions. It should be noted that the density and energy populations are related through the EOS, which describes the relationship between the thermodynamic properties of the fluid. Fig. 14 displays the effect of the outlet temperature reduction on the mass flow rate for the adiabatic, isothermal, and diabatic descriptions. Based on the adiabatic prediction, the point at which the mass flow rate experiences a kink is shifted towards a smaller relative inlet pressure. However, for the diabatic description, the capillary condensation happens for larger relative inlet pressure. In Fig. 14, when the relative inlet pressure is approximately 0.88, capillary condensation causes an increase in the mass flow rate in the adiabatic analysis. The adiabatic prediction for a relative inlet pressure of $p_{\text{in,r}} \approx 0.94~p_{\text{sat}}$ indicates a mass flow rate that is 80~% larger compared to the isothermal analysis. The shift of the location where evaporation occurs can be attributed to the effect of temperature field. Fig. 15 shows the temperature and pressure distribution for $p_{\text{in,r}} = 0.97$ according to the isothermal, adiabatic and diabatic descriptions. It is important to note that the radius of the upstream meniscus in the isothermal prediction is larger than the radius of the upstream curve in the adiabatic and diabatic descriptions; see the density contour plotted in Fig. 15c. As a result, for the mentioned relative inlet pressure, the pressure difference across the upstream meniscus increases for the adiabatic prediction compared to the isothermal description, as shown in the pressure distribution plotted in Fig. 15, leading to a decrease in the mass flow rate. However, with the adiabatic downstream boundary condition, the temperature reduction, see Fig. 15b, is a reason to increase the mass flow rate. Regarding the computation with the diabatic boundary condition, the temperature at the inlet of the nano-slit is larger than that of the isothermal description; see Fig. 15b. Additionally, the diabatic analysis's pressure difference across the inlet meniscus is larger than that of the isothermal description; see Fig. 15a. Consequently, the mass flow rate decreases in the diabatic description compared to the isothermal prediction for the same relative inlet pressure.

5. Conclusion

This study utilized the thermal two-phase lattice Boltzmann method to investigate nanoscale fluid dynamics and phase change phenomena within confined nanoslits. The situation at the downstream meniscus was specifically investigated, and it was found that the pressure difference across the meniscus decreases with increasing mass flow rate. However, a geometrical analysis of the downstream meniscus shows that the decrease of the pressure is entirely due to a different shape of the meniscus with a larger radius of curvature. Regardless of mass transfer across the meniscus, the Young-Laplace equation is very well obeyed at the interface for all flow situations. The radius of curvature is influenced by the adhesive strength and the formation of an adsorbed layer downstreams of the meniscus, showing that the lattice Boltzmann method presented here is able to simulate a flow where surface tension and fluid-wall interactions are of importance.

The effects of temperature conditions could also be reproduced with the method presented here. Under adiabatic conditions at the downstream boundary, the kink point where the mass flow rate increases moves to smaller inlet pressure while for diabatic boundary conditions, i.e, the outlet temperature is set equal to the inlet temperature, the kink point occurs for larger relative inlet pressures.

Other effects that are known from classical continuum descriptions were also observed using the lattice Boltzmann method: With decreasing slit width, the effect of condensation on the mass flow rate becomes larger. Regarding the effect of adhesive strength, stronger adhesive forces change the meniscus curvature by effectively decreasing the contact angle, leading to increased capillary pressure and subsequent enhancements in the length of the liquid phase.

CRediT authorship contribution statement

Javad Sodagar-Abardeh: Writing – review & editing, Writing – original draft, Visualization, Validation, Software, Methodology; **Thomas Loimer:** Writing – review & editing, Supervision.

Data Availability

The simulation data and source code used in this study are available in the Zenodo repository at the following link: https://doi.org/10.5281/zenodo.15281344

Declaration of competing interest

The authors declare that they have no known competing financial interests or personal relationships that could have appeared to influence the work reported in this paper.

Acknowledgement

This research was funded in whole or in part by the Austrian Science Fund (FWF) [10.55776/14816]. For open access purposes, the author has applied a CC BY public copyright license to any author accepted manuscript version arising from this submission.

Supplementary material

Supplementary material associated with this article can be found in the online version at 10.1016/j.ces.2025.121935

References

Albernaz, D., Do-Quang, M., Amberg, G., 2015. Multirelaxation-time lattice Boltzmann model for droplet heating and evaporation under forced convection. Phys. Rev. E 91 (4), 043012.

Areshi, M., Tseluiko, D., Thiele, U., Goddard, B.D., Archer, A.J., 2024. Binding potential and wetting behavior of binary liquid mixtures on surfaces. Phys. Rev. E 109 (2), 024801.

Bao, J., Guo, Z., 2024. Phase-field lattice Boltzmann model with singular mobility for quasi-incompressible two-phase flows. Phys. Rev. E 109 (2), 025302.

Choi, J.-G., Do, D.D., Do, H.D., 2001. Surface diffusion of adsorbed molecules in porous media: monolayer, multilayer, and capillary condensation regimes. Ind. Eng. Chem. Res. 40, 4005–4031.

- Cueto-Felgueroso, L., Fu, X., Juanes, R., 2018. Pore-scale modeling of phase change in porous media. Phys. Rev. Fluids 3 (8). 084302.
- Deng, J., Zhang, Q., Zhang, L., Lyu, Z., Rong, Y., Song, H., 2023. Investigation on the adsorption properties and adsorption layer thickness during CH4 flow driven by pressure gradient in nano-slits. Phys. Fluids 35 (1), 016104.
- Edison, J.R., Monson, P.A., 2012. Dynamic mean field theory of condensation and evaporation in model pore networks with variations in pore size. Microporous Mesoporous Mater. 154, 7–15
- Edison, J.R., Monson, P.A., 2013. Dynamic mean field theory for lattice gas models of fluid mixtures confined in mesoporous materials. Langmuir 29 (45), 13808–13820.
- Fei, L., Qin, F., Wang, G., Luo, K.H., Derome, D., Carmeliet, J., 2022. Droplet evaporation in finite-size systems: theoretical analysis and mesoscopic modeling. Phys. Rev. E 105 (2), 025101.
- Huang, H., Krafczyk, M., Lu, X., 2011. Forcing term in single-phase and Shan-Chen-type multiphase lattice Boltzmann models. Phys. Rev. E 84 (4), 046710.
- Huang, J., Yin, X., Barrufet, M., Killough, J., 2021. Lattice Boltzmann simulation of phase equilibrium of methane in nanopores under effects of adsorption. Chem. Eng. J. 419, 129625.
- Jin, Z., Firoozabadi, A., 2016. Thermodynamic modeling of phase behavior in shale media. SPE J. 21 (01), 190–207.
- Kamali, M.R., Gillissen, J.J.J., Van den Akker, H.E.A., Sundaresan, S., 2013. Lattice-Boltzmann-based two-phase thermal model for simulating phase change. Phys. Rev. E 88 (3), 033302.
- Khadem, S.A., Jahromi, I.R., Zolghadr, A., Ayatollahi, S., 2014. Pressure and temperature functionality of paraffin-carbon dioxide interfacial tension using genetic programming and dimension analysis (GPDA) method. J. Nat. Gas Sci. Eng. 20, 407–413.
- Khadem, S.A., Rey, A.D., 2021. Nucleation and growth of cholesteric collagen tactoids: a time-series statistical analysis based on integration of direct numerical simulation (DNS) and long short-term memory recurrent neural network (LSTM-RNN). J. Colloid Interface Sci. 582, 859–873.
- Kupershtokh, A.L., Medvedev, D.A., 2006. Lattice Boltzmann equation method in electrohydrodynamic problems. J. Electrostat. 64 (7–9), 581–585.
- Lee, K.H., Hwang, S.T., 1986. The transport of condensible vapors through a microporous vycor glass membrane. J. Colloid Interface Sci. 110 (2), 544–555.
- Li, Z., Firoozabadi, A., 2009. Interfacial tension of nonassociating pure substances and binary mixtures by density functional theory combined with Peng–Robinson equation of state. J. Chem. Phys. 130 (15), 154108.
- Li, Z., Jin, Z., Firoozabadi, A., 2014. Phase behavior and adsorption of pure substances and mixtures and characterization in nanopore structures by density functional theory. SPE J. 19 (06), 1096–1109.
- Liu, Y., Jin, Z., Li, H.A., 2018. Comparison of Peng-Robinson equation of state with capillary pressure model with engineering density-functional theory in describing the phase behavior of confined hydrocarbons. SPE J. 23 (05), 1784–1797.
- Loimer, T., Podgolin, S.K., Sodagar-Abardeh, J., Petukhov, D.I., Eliseev, A.A., 2023. Influence of heat transfer and wetting angle on condensable fluid flow through nanoporous anodic alumina membranes. Phys. Chem. Chem. Phys. 25, 3240–3250.
- Loimer, T., Setnickova, K., Uchytil, P., 2019. Consideration of the joule-Thomson effect for the transport of vapor through anodic alumina membranes under conditions of capillary condensation. Sep. Purif. Technol. 215, 548–556.
- Loimer, T., Uchytil, P., Petrickovic, R., Setnickova, K., 2011. The flow of butane and isobutane vapors near saturation through porous vycor glass membranes. J. Membr. Sci. 383 (1–2), 104–115.
- Monson, P.A., 2012. Understanding adsorption/desorption hysteresis for fluids in mesoporous materials using simple molecular models and classical density functional theory. Microporous Mesoporous Mater. 160, 47–66.

- Namadchian, H., Sodagar-Abardeh, J., Arabkoohsar, A., Ismail, K.A.R., 2022. Numerical investigation of simultaneous effects of nanofluid flow and porous baffle on thermal energy transfer and flow features in a circular channel. J. Energy Resour. Technol. 144 (2), 022102.
- Pasieczynski, K., Chen, B., 2020. Multipseudopotential interaction models for thermal lattice Boltzmann method simulations. Phys. Rev. E 102 (1), 013311.
- Phan, A., Fan, D., Striolo, A., 2020. Fluid transport through heterogeneous pore matrices: multiscale simulation approaches. Phys. Fluids 32 (10), 101301.
- Qin, F., Del Carro, L., Moqaddam, A.M., Kang, Q., Brunschwiler, T., Derome, D., Carmeliet, J., 2019. Study of non-isothermal liquid evaporation in synthetic micro-pore structures with hybrid lattice Boltzmann model. J. Fluid Mech. 866, 33-60.
- Rathi, A., Kikkinides, E.S., Ford, D.M., Monson, P.A., 2019. Nonequilibrium steady states in fluid transport through mesopores: dynamic mean field theory and nonequilibrium molecular dynamics. Langmuir 35 (17), 5702–5710.
- Sodagar-Abardeh, J., Asadollahi, A., Loimer, T., 2023. Mesoscale simulation of the equilibrium state of the confined nanoscale two-phase flow in the presence of corner interface and adsorbed liquid layer. Chem. Eng. Sci. 270, 118563.
- Song, Z., Song, Y., Guo, J., Zhang, Z., Hou, J., 2020. Adsorption induced critical shifts of confined fluids in shale nanopores. Chem. Eng. J. 385, 123837.
- Succi, S., 2002. Mesoscopic modeling of slip motion at fluid-solid interfaces with heterogeneous catalysis. Phys. Rev. Lett. 89 (6), 064502.
- Sun, Z., Li, X., Liu, W., Zhang, T., He, M., Nasrabadi, H., 2020. Molecular dynamics of methane flow behavior through realistic organic nanopores under geologic shale condition: pore size and kerogen types. Chem. Eng. J. 398, 124341.
- Uchytil, P., Petrickovic, R., Seidel-Morgenstern, A., 2005. Study of capillary condensation of butane in a vycor glass membrane. J. Membrane Sci. 264 (1–2), 27–36.
- Uchytil, P., Petrickovic, R., Thomas, S., Seidel-Morgenstern, A., 2003. Influence of capillary condensation effects on mass transport through porous membranes. Sep. Purif. Technol. 33 (3), 273–281.
- Wang, S.-C., Tong, Z.-X., He, Y.-L., Liu, X., 2022. Unit conversion in pseudopotential lattice Boltzmann method for liquid-vapor phase change simulations. Phys. Fluids 34 (10), 103305.
- Wang, Y., Aryana, S.A., 2021. Coupled confined phase behavior and transport of methane in slit nanopores. Chem. Eng. J. 404, 126502.
- Yabunaka, S., Fujitani, Y., 2022. Isothermal transport of a near-critical binary fluid mixture through a capillary tube with the preferential adsorption. Phys. Fluids 34 (5), 052012
- Yu, H., Fan, J., Chen, J., Zhu, Y., Wu, H., 2018. Pressure-dependent transport characteristic of methane gas in slit nanopores. Int. J. Heat Mass Transf. 123, 657–667.
- Yuan, P., Schaefer, L., 2006. Equations of state in a lattice Boltzmann model. Phys. Fluids 18 (4), 042101.
- Zarghami, A., Van den Akker, H.E.A., 2017. Thermohydrodynamics of an evaporating droplet studied using a multiphase lattice Boltzmann method. Phys. Rev. E 95 (4), 043310
- Zarghami, A., Looije, N., Van den Akker, H., 2015. Assessment of interaction potential in simulating nonisothermal multiphase systems by means of lattice Boltzmann modeling. Phys. Rev. E 92 (2), 023307.
- Zarragoicoechea, G.J., Kuz, V.A., 2004. Critical shift of a confined fluid in a nanopore. Fluid Phase Equilib. 220 (1), 7–9.
- Zou, Q., He, X., 1997. On pressure and velocity boundary conditions for the lattice Boltzmann BGK model. Phys. Fluids 9 (6), 1591–1598.